

Original Research

Core Ideas

- Infiltration experiments were conducted on a sample under two boundary conditions.
- Time-lapse neutron imaging was used to determine water distribution in the sample.
- Significant air entrapment was detected in the case of slow drip irrigation infiltration.
- Gravity-driven ponding infiltration led to much less air entrapment.
- Air entrapment led to one order of magnitude lower conductivity in the case of drip irrigation.

J. Sacha and M. Snehota, Faculty of Civil Engineering, Czech Technical Univ. in Prague, Thakurova 7, Prague 6, 166 29, Czech Republic; M. Snehota, Univ. Centre for Energy Efficient Buildings, Czech Technical Univ. in Prague, Trinecka 1024, Bustehrad, 273 43, Czech Republic; P. Trtik and J. Hovind, Lab. for Neutron Scattering and Imaging, Paul Scherrer Institut, 5232 Villigen PSI, Switzerland. *Corresponding author (michal.snehota@fsv.cvut.cz).

Received 11 Jan. 2019.
Accepted 3 June 2019.

Citation: Sacha, J., M. Snehota, P. Trtik, and J. Hovind. 2019. Impact of infiltration rate on residual air distribution and hydraulic conductivity. *Vadose Zone J.* 18:190003. doi:10.2136/vzj2019.01.0003

© 2019 The Author(s). This is an open access article distributed under the CC BY-NC-ND license (<http://creativecommons.org/licenses/by-nc-nd/4.0/>).

Impact of Infiltration Rate on Residual Air Distribution and Hydraulic Conductivity

Jan Sacha, Michal Snehota,* Pavel Trtik, and Jan Hovind

The dynamics of water infiltration into soil have a strong influence on the subsequent distribution of air trapped inside pores. We present results of two infiltration experiments conducted on an artificially prepared sample under ponding and drip irrigation boundary conditions, with concurrent neutron imaging of the sample. A cylindrical sample was packed with two grades of sand and disks of fine porous ceramic in an axially symmetrical geometry. The configuration of the sample provided a number of interfaces between regions of higher and lower hydraulic conductivity. Infiltration was started in dry media. The bottom boundary condition was seepage face. Water was applied on the sample surface during the experiment with drip irrigation at a water application rate about one order of magnitude lower than the minimum flux reached during the ponding experiment. Despite this low application rate, ponding eventually occurred on the top of the sample due to an unexpectedly low infiltration rate. Neutron tomographic imaging revealed massive air entrapment in the coarse sand regions of the sample during slow infiltration under drip irrigation conditions. In contrast, during the ponded infiltration experiment, the air was mostly flushed out from the coarse sand regions by gravity-driven water flow due to greater hydraulic head. Neutron imaging showed that the capillary barrier effect, air entrapment, and entrapped air redistribution were responsible for the observed low infiltration capacity of the sample during the slow-infiltration-dominated drip irrigation experiment. It is reasonable to assume that similar phenomena can occur in natural soils having highly heterogeneous structures.

Abbreviations: BOA, Beamline for Neutron Optics and Other Approaches; CTU, Czech Technical University; DE, drip irrigation infiltration experiment; NEUTRA, Neutron Transmission Radiography; NI, neutron imaging; PE, ponded infiltration experiment; PSI, Paul Scherrer Institut; VGM, van Genuchten–Mualem.

Richards' equation, which is widely applied to model variable flow through porous media such as soil, neglects the air phase (Richards, 1931). However, in many cases air has a strong influence on water flow (e.g., Christiansen, 1944; Faybishenko, 1995). For example, when entrapped air blocks water flow in pores, infiltration is significantly slower than expected. Uneven wetting or drainage fronts can affect air entrapment when the wetting front bypasses air-filled regions and encapsulates the air in them (e.g., Szymańska et al., 2016).

In general, uneven wetting or drainage fronts occur due to (i) reduced wettability, (ii) the spatial variability of hydraulic conductivity, and (iii) the effects of air-entry barriers. Silliman et al. (2002), who investigated water table fluctuations in a laboratory experiment, emphasized the importance of air-entry barriers. They reported that regions of coarse sand embedded in fine sand remained fully saturated although the water level dropped below the coarse sand inclusion and its theoretical capillary height. They hypothesized that the region of fine sand overlying the coarse sand acted as an air-entry barrier and prevented air from entering the coarse sand, thus preventing its drainage. A similar effect was observed by Kuang et al. (2011), who investigated drainage of water from coarse sand columns with and without the inclusion of a thick layer of fine sand at the top. During the drainage experiment, the pressure immediately below the fine sand layer decreased to a minimum value of -2.5 kPa and then, once the air-entry pressure of the fine sand was exceeded, the tension disappeared. The opposite effect of the air-entry barrier was investigated by Szymańska et al. (2016), who performed an infiltration into fine sand that contained a

coarse sand inclusion. A significant amount of air was trapped in the coarse sand because of the formation of an air-entry barrier.

The capillary barrier effect occurs at the interface between fine porous media overlying coarse porous media. Water flow across the interface is then prevented due to low capillary forces in the coarse material. The capillary barrier effect has been used in engineering practice, e.g., to protect waste storage from rain-water leaching (Ray et al., 2010). The capillary barrier effect can be successfully simulated using both a multiphase flow approach (Oldenburg and Pruess, 1993) or a single-phase approach based on Richards' equation (Prédélus et al., 2015).

In periodically wetted heterogeneous soils, both air-entry and capillary barriers may naturally be present and influence the shape of the wetting front during infiltration. It was hypothesized by Faybishenko (1995) that air entrapment in near-saturated soil is much more pronounced in heterogeneous soils, particularly due to uneven wetting fronts. An example of soils prone to air entrapment are soils from Cambisol series formed on gneiss. Using magnetic resonance imaging, Sněhota et al. (2010) detected entrapped air bubbles in samples of a Cambisol characterized by high heterogeneity and a broad range of pore sizes. Scanning electron microscope images (Fig. 1) show an example of a common Cambisol soil that contains four distinct domains characterized by pore size distribution: (i) compact stones with very little porosity, (ii) the soil matrix, and (iii) a system of larger pores of sub-millimeter size that are often interrupted by (iv) narrow pore necks or the soil matrix. Such heterogeneity can lead to the formation of an uneven wetting front.

The term *quasi-saturated soil* was introduced by Faybishenko (1995) to describe the state in which air is trapped in soil but not connected to the atmosphere. The terms *satiated* or *field-saturated hydraulic conductivity* are also used to describe conditions of otherwise saturated soil containing entrapped air in soil pores (e.g., Reynolds and Elrick, 1986).

Air entrapment occurs during infiltration when air is gradually pushed downward to the lower soil layers by infiltrating water

(Christiansen, 1944; Debacker, 1967) and becomes disconnected from the atmosphere. In addition, gas bubbles and clusters (more interconnected air-filled pores) can evolve directly in pores due to many other processes, including microbial activity (Soares et al., 1988), depressurization (Tsimpanogiannis and Yortsos, 2002), chemical reactions (Zhang and Gillham, 2005), or during artificial air sparging (Roosevelt and Corapcioglu, 1998). From the examples above, it is evident that trapped gas may be present in otherwise saturated soils. The presence of entrapped air in near-saturated soil decreases the hydraulic conductivity both on a sample scale (e.g., Christiansen, 1944; Faybishenko, 1995; Sněhota et al., 2015; Šácha and Sněhota, 2016) and on a field scale (Zlotnik et al., 2007; Loizeau et al., 2017) and has an influence on the transport of contaminants and on various biochemical processes (Yakirevich et al., 2010). Air can become retained by means of structural trapping (Szymańska et al., 2016), where air is being trapped due to soil heterogeneity and pore-scale capillary trapping (Geistlinger et al., 2015). Entrapped air effects on flow rate cannot be simulated using models based on the single-phase Richards equation because of the neglected air phase unless the entrapped air regions are inserted artificially into the flow domain, for example as no-flow regions (Dohnal et al., 2013). It can be concluded that the mechanisms of air entrapment in soils are not yet sufficiently understood.

For detailed investigation of processes in opaque media such as soil, it is convenient to visualize water behavior using nondestructive imaging methods. One such method is neutron imaging (NI), which utilizes the ability of a neutron beam to interact with materials. Perfect et al. (2014) provide an extensive review of the use of NI methods in the study of geomaterials. The utility of this method in the investigation of flow and transport processes in various porous media was earlier demonstrated by Lehmann et al. (2006). Likewise, Kaestner et al. (2016) recently published a review of recent developments in NI for porous media research. They showed that tomography imaging of the processes in the rhizosphere with a pixel size of 45 μm was feasible with a tomography scan time of 30 s.

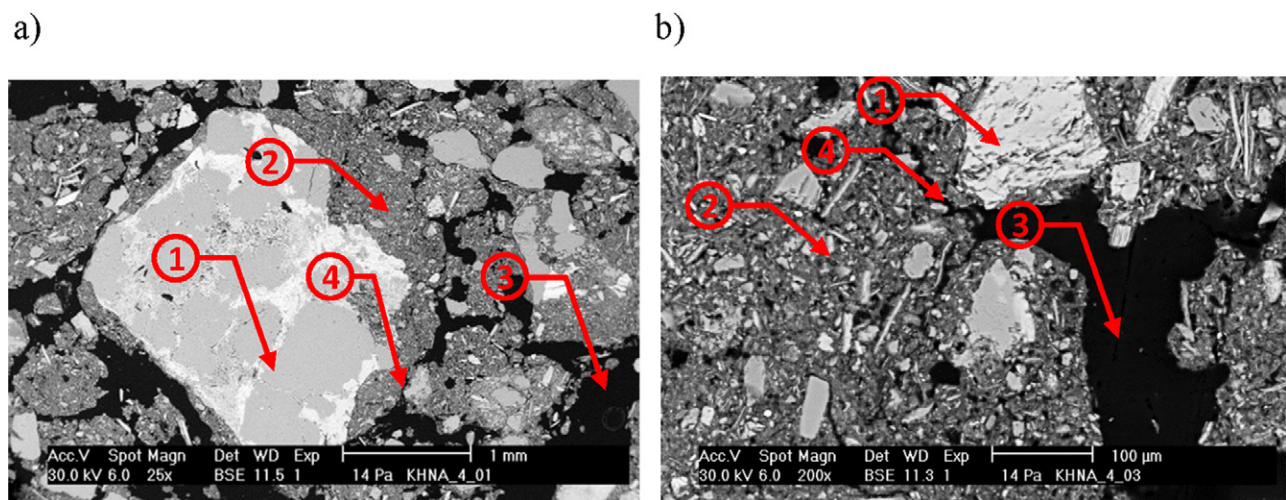


Fig. 1. Scanning electron microscope image of resin-impregnated sample of Cambisol soil formed on weathered gneiss at (a) 25 \times and (b) 200 \times magnification. Numbers refer to four distinct domains of stones (1), soil matrix (2), larger pores (3), and narrow necks of larger pores (4).

Because of the strong attenuation of neutrons by H, and the low attenuation of neutrons by the majority of other soil components, NI is suitable for investigations of water transport in soil. Neutron imaging has been widely used to study flow processes in the rhizosphere (e.g., Menon et al., 2007; Moradi et al., 2009; Oswald et al., 2008; Zarebanadkouki et al., 2014), monitor flow in heterogeneous soils with biopores (Badorreck et al., 2010, 2012, 2013), examine evaporation from porous media (e.g., Shokri et al., 2010) and flow in soil aggregates (Carminati et al., 2007), and study water flow dynamics in heterogeneous porous media (Vasin et al., 2008; Schaap et al., 2008). Hassanein et al. (2006b) studied the infiltration into various types of porous stone using neutron radiography. Using NI, Cheng et al. (2012) successfully determined the main drying and wetting branches of the retention curves of sand samples. Snehota et al. (2015) used NI to investigate the effect of trapped air redistribution on the quasi-saturated hydraulic conductivity of a heterogeneous assembled sample. The available temporal resolution of NI was recently enhanced significantly due to advancement of the NI technology (more sensitive detectors, higher beam intensities, novel image processing), thus enabling the imaging of dynamic processes. For example, Zboray and Trtik (2018) reported radiography imaging of the air–water interface (without the porous media) at 800 frames per second. Neutron imaging is clearly a powerful advancing technique but needs to be used carefully to obtain quantitative data on water contents. Hassanein et al. (2006a) and de Beer and Middleton (2006) noted the difference between NI-derived water content and the results of gravimetric measurements of water content and suggested the need for image corrections to resolve various artifacts in NI.

Because of the complexity of natural soils' pore network geometry and chemical properties, it is convenient to study individual processes on simpler media with inert chemical properties and a well-defined pore geometry that is stable with time. The effects of heterogeneity have often been investigated experimentally in the laboratory on artificially prepared samples (Silliman et al., 2002; Dunn and Silliman, 2003; Vasin et al., 2008; Szymkiewicz et al., 2012). Conducting these experiments on a medium with known inner geometry reduces the uncertainties of analyses and modeling.

To our knowledge, no study has been done on how the infiltration rate affects the amount of entrapped air in the soil using

imaging and suppression of the other possible effects like pore geometry alterations and the influence of the initial water content. The aim of our study was to utilize contemporary NI techniques to quantitatively assess the influence of the infiltration rate on the amount of subsequent air entrapment. Specifically, our focus was on identifying regions prone to air entrapment. At this stage, we aimed at performing the infiltration experiments to study air entrapment on carefully designed heterogeneous porous media with relatively simple, axially symmetric geometry that in principle resemble real heterogeneous soils (e.g., the soil shown in Fig. 1) but with much less complex geometry. The research question was how much the air-entry barrier effect influences air entrapment in specifically designed samples of heterogeneous porous media.

Materials and Methods

Sample

Experiments were conducted on a sample constructed of two distinct sands and fine-grained ceramic disks packed into a quartz glass tube to produce an axially symmetrical inner geometry in which the ceramic disks were surrounded by the two coarser sands (Fig. 2).

The sample composition, despite being artificial, reflects the composition of some soils. For example a functionally similar arrangement, characterized by a finer material embedded in coarser material, can be found in soils with a content of larger grains, where porous stones or the soil matrix are surrounded by coarser weathered material, or in aggregated soils in which stable, porous aggregates are surrounded by interaggregate voids. To additionally enhance air entrapment in the sample, we interlaced the layers of coarse sand with a medium sand at three heights.

Two sands of different particle size fractions were used to construct the sample. These were quartz sand FH31 (Quarzwirke GmbH), a commercial product with standardized chemical and physical characteristics and a high chemical purity. Two types FH31 sand were produced for the sample packing (Table 1). Whole FH31 sand will hereafter be referred to as coarse sand, while the part of FH31 < 0.4 mm obtained by dry sieving of FH31 sand with a 0.4-mm sieve will be referred to as medium sand. The particle size analysis of both sands is presented in Table 1.

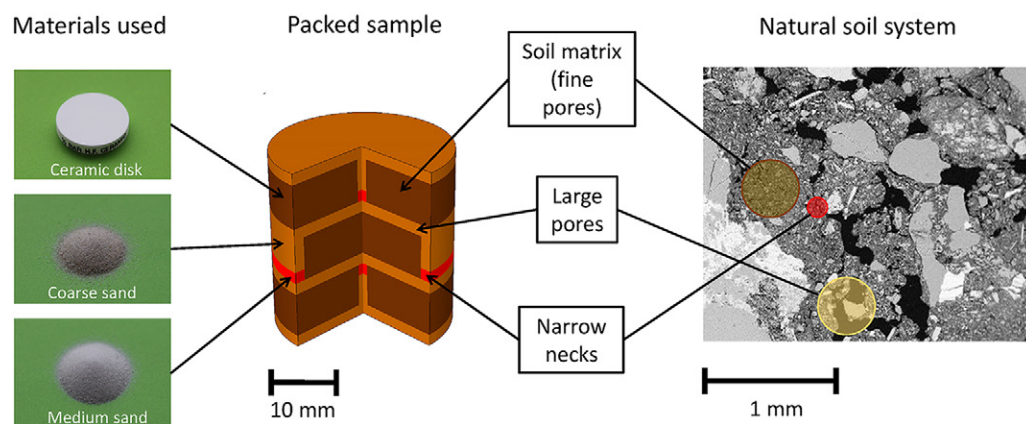


Fig. 2. Design of the sample geometry. Three materials were used to construct the sample: ceramic disks (two of them drilled in the middle) representing the soil matrix and coarse and medium sand representing the domain of larger pores and narrow necks on large pores. The sample's diameter is 29.0 mm and its height is 39.0 mm.

Table 1. The van Genuchten parameters of the retention curves, saturated hydraulic conductivity, and grain size distribution of three materials used to build a composited sample.

Property	Ceramic disks	Coarse sand	Medium sand
Parameters determining shape of retention curve (van Genuchten, 1980)			
Saturated water content (θ_s), $\text{cm}^3 \text{cm}^{-3}$	0.585	0.408	0.476
Residual water content (θ_r), $\text{cm}^3 \text{cm}^{-3}$	0.000	0.028	0.021
Empirical parameter α , cm^{-1}	8.0×10^{-4}	3.7×10^{-2}	3.1×10^{-2}
Empirical parameter n	3.536	5.913	2.295
Saturated hydraulic conductivity (K_s), cm h^{-1}	0.11†	144.00	26.14
Bulk density (ρ_v), g cm^{-3}	1.58	1.71	1.66
Particle size			
Very coarse sand fraction (1.0–1.2 mm), %	–	0.03	0.00
Coarse sand fraction (0.5–1.0 mm), %	–	5.95	0.03
Medium sand fraction (0.25–0.5 mm), %	–	54.33	14.58
Fine sand fraction (0.1–0.25 mm), %	–	24.10	71.43
Very fine sand fraction (0.10–0.25 mm), %	–	12.67	11.05
Silt fraction (0.002–0.05 mm), %	–	2.93	2.93
Maximum pore diameter, μm	6	–	–

† Saturated hydraulic conductivity of the ceramic disks as reported by the manufacturer (Soilmoisture Equipment Corp.).

High-flow porous ceramic disks with a 50-kPa (0.5-bar) air-entry value (Soilmoisture Equipment Corp.) were used to represent a fine-grained, least permeable material in the sample. The disks were machined to the required diameters, and two of them were carefully drilled through the center.

The grain size distribution, retention curve, and saturated conductivity of all three materials were characterized in the laboratory. A combination of the Casagrande hydrometer (Casagrande, 1934) and sieving methods was used to determine the particle size distributions of the sand types. The main drainage branch of the retention curves was determined using the standard sand box and pressure extractor (Soilmoisture Equipment Corp.) instrumentation and method (Klute, 1986). The measurements were conducted in triplicate on homogeneously packed samples of sand and on the porous ceramic disks. Then, the van Genuchten parameters of the retention curve (van Genuchten, 1980) residual and saturated water content (θ_r and θ_s , respectively) and fitting parameters α and n were determined by the nonlinear least-squares method from measured retention data points using the RETC code (van Genuchten et al., 1991). Figure 3 shows the significant difference between the shapes of the retention curves of the three materials. It is easily visible that the ceramic disks drain at significantly higher pF values than the sands.

The saturated hydraulic conductivity of the sands was measured in the laboratory using the constant gradient method. The saturated hydraulic conductivity and maximum pore size of the ceramic disks were provided by the manufacturer. Table 1

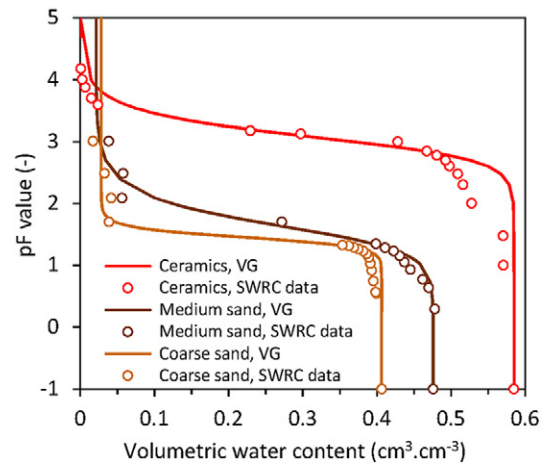


Fig. 3. Soil water retention curve (SWRC) as volumetric water content θ vs. pF value ($pF = \log_{10}[h_w]$, where h_w is the pressure head in centimeters of water column) for the three materials used in the study. Data points are shown as circles, lines represent fitted van Genuchten (VG) model using the RETC code (van Genuchten et al., 1991).

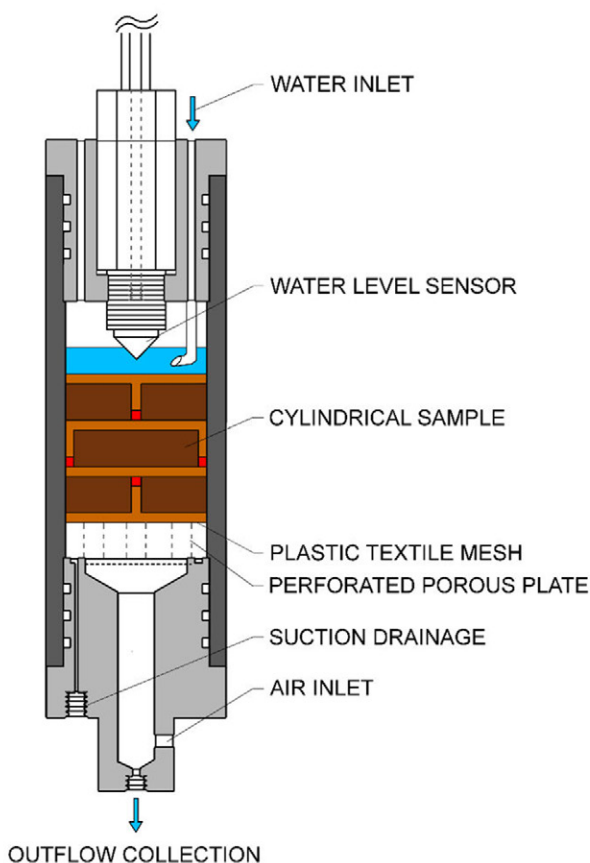
provides an overview of the van Genuchten parameters of the retention curves and the main physical properties of the materials. As verified by the water drop penetration time test (Dekker et al., 1998), none of three materials exhibited water repellency in a dry condition after drying in an oven at 60°C to constant weight.

The sample was carefully assembled in a quartz glass tube and capped with fittings on both ends. The inner diameter of the tube was 29.0 mm and its height was 39.0 mm. Figure 4 is a schematic of the sample along with the sample holder. The sample is supported by the plastic textile mesh placed on the top of a porous ceramic plate in which 14 holes, each 3.5-mm diameter, were drilled to allow conduction of high water fluxes. The perforated porous plate was made of porous ceramic with a 0.1-MPa (1-bar) air-entry value (Soilmoisture Equipment Corp.). This setup also allows application of tension to the bottom of the sample, but this option was not utilized in the current study. Therefore water was allowed to flow freely through the bottom of the sample through holes in the perforated porous plate.

Experiments

Drip irrigation infiltration (DE) and ponded infiltration experiments (PE) using heavy water (D_2O) were conducted on the sample, once with concurrent neutron imaging. The term *drip irrigation* in DE refers to the mean of water application, i.e., slow, uninterrupted water delivery at a constant flow rate. As shown below, a ponding condition developed also in the DE experiment. The purpose of the NI was to determine the water spatiotemporal distribution in the sample during water flow under different boundary conditions. The initial condition for all experiments was an oven-dry sample, dried at 60°C to constant weight. Drying was speeded up by exposing the sample to dry air, delivered by a small aquarium air pump at an approximate flow rate of 100 L h⁻¹

Ponding infiltration



Drip irrigation

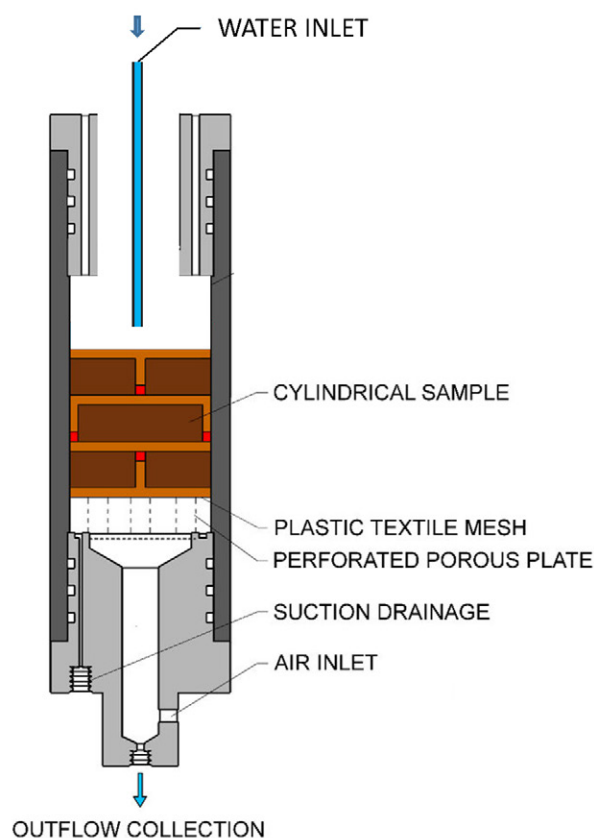


Fig. 4. Schematic of the sample holder assembly as it was used in the ponding infiltration experiment (PE) and drip irrigation infiltration experiment (DE).

through the column of desiccant (Laboratory Gas Drying Unit, Calcium Sulfate, Drierite) directly in the oven. The absence of water was then carefully checked also by neutron radiography in which even minute traces of H_2O would produce an easily visible contrast gradient between the ceramic disks.

The advantage of starting infiltration with a dry sample is that a reference NI tomogram can be obtained, which then allows the quantification of water content in the sample in succeeding tomograms. The air content of the heavy water was well equilibrated with atmospheric pressure before the experiments.

Two DE and two PE replicated experiments were performed in the laboratory without imaging (see the experiment schedule in Table 2) with aerated H_2O . The same number of replicated experiments were also performed using degassed water without imaging. The purpose of using degassed water was to dissolve the entrapped air to determine the hydraulic conductivity of the fully saturated sample.

Neutron Imaging of Infiltration–Outflow Experiments

Heavy water (D_2O) was used in the experiments monitored by neutron imaging at the beamline facilities of the Paul Scherrer

Institute, Swiss Spallation Neutron Source (Fischer, 1996). Water was kept in a loosely covered vessel; therefore the dissolved air partial pressure was in equilibrium with atmospheric pressure, a state we will refer to as *aerated water*. A peristaltic pump delivered water to the center of the upper surface of the sample.

For the DE, 0.03 mL of heavy water was delivered every 10 s for 1.5 h, which corresponded to an infiltration rate of 1.63 cm h^{-1} (with respect to the cross-sectional area of the sample, 6.61 cm^2). Water was delivered to the center point of the sample surface by 0.318-cm (1/8-inch) tubing.

For the PE, an initial dose of 5.0 mL was delivered during the first 5 s of the experiment to quickly produce ponding across the sample surface. A constant ponding depth of about 6 mm was then maintained using an optical water level sensor (LV171, Omega Engineering). Each time the water level dropped by approximately 1 mm, another dose of 0.85 mL was delivered, which corresponds to a water height of approximately 1.3 mm. The ponding infiltration was maintained for 16 h.

The water was allowed to flow freely by gravity through the perforated disk at the bottom of the sample. The amount of inflow and outflow was recorded gravimetrically using digital balances with 0.01-g resolution.

Table 2. Experimental schedule for this study.

Parameter	Facility†	Beamline‡	Boundary condition of experiments§	Neutron imaging		No. of replicates	Notes
				2D (radiography)	3D (tomography)		
With neutron imaging	PSI	BOA	DE	–	transient and steady-state flow phases	1	aerated D ₂ O water
		NEUTRA	PE	transient flow phase	steady-state flow phase	1	
Without neutron imaging	CTU		DE			2	aerated H ₂ O water
			PE			2	
			DE			2	degassed H ₂ O water
			PE			2	

† PSI, Paul Scherrer Institut; CTU, Czech Technical University.

‡ BOA, Beamline for Neutron Optics and other Approaches; NEUTRA, Neutron Transmission Radiography.

§ DE, drip irrigation infiltration experiment; PE, ponding infiltration experiment.

The sample was imaged at two different neutron beamlines at the Paul Scherrer Institut (PSI). The PE sample was imaged at the Neutron Transmission Radiography (NEUTRA) beamline (Lehmann et al., 2001), whereas the DE sample was imaged about 1 yr later at the Beamline for Neutron Optics and Other Approaches (BOA) (Morgano et al., 2014). Different imaging strategies were used to capture the transient part of the infiltration in each case. Two-dimensional imaging (neutron radiography) of the transient part of the experiment was performed during ponded infiltration at the NEUTRA beamline because the process was too fast for any three-dimensional neutron imaging technique, including the recently enabled ultra-fast state-of-the-art neutron tomography (Tötzke et al., 2017). For the much slower DE, it was decided to use the fast on-the-fly, three-dimensional neutron tomographic imaging at the BOA (Zarebanadkouki et al., 2015) during which samples are rotated along the vertical axis. For the PE and DE, the three-dimensional neutron imaging was performed on the dry sample, on the wetted sample after steady state flow was reached, and on the fully saturated sample. An overview of the neutron imaging parameters is given in Table 3.

Image Analysis

All raw neutron radiographs were normalized for background noise and for spatial inhomogeneities of the detector, for temporal fluctuations of the neutron flux, and for spatial inhomogeneities of the neutron beam. Normalized radiographs taken during the infiltrations were divided by radiographs of the dry sample taken at a corresponding angle. Thus, two-dimensional water thickness maps were obtained. Corrections of the neutron-derived water thickness maps were applied because it was considered likely that the outcome could be affected by beam hardening and neutron scattering artifacts. A simple empirical correction based on the method developed by Kang et al. (2013) was used to calculate the corrected water thickness in the projections. The image processing path was described in detail by Šácha and Sněhota (2016). Water thickness in each pixel of the projection image, empirically corrected for beam hardening and neutron scattering, was calculated as

$$d_w = \sqrt{\frac{-\ln(I_{\text{DRY}}/I_{\text{WET}})}{\beta} + \left(\frac{\Sigma_w}{2\beta}\right)^2} - \frac{\Sigma_w}{2\beta} \quad [1]$$

where d_w (cm) is the thickness of the water in the direction perpendicular to the detector plane, I_{DRY} (arbitrary units) is the normalized pixel intensity in an image of dry sample, I_{WET} (arbitrary units) is the normalized pixel intensity in an image during the experiment, Σ_w (cm⁻¹) is the attenuation coefficient of the water, and β (cm⁻²) is the beam hardening correction parameter. The values of Σ_w and β were calculated (for the DE: $\Sigma_w = 0.75$ cm⁻¹ and $\beta = 0.075$ cm⁻²; for the PE: $\Sigma_w = 0.71$ cm⁻¹ and $\beta = 0.075$ cm⁻²) by optimization to minimize the residuals between the amount of water actually delivered to the sample and the amount of water detected in the image in each time step during the first 58 and 167 radiographs for the DE and PE experiments, respectively.

Three-dimensional series' of tomograms of the water content distribution in the samples were reconstructed from projections representing the water thickness by the filtered back-projection reconstruction algorithm using MuhRec computer tomography reconstruction software (Kaestner, 2011).

For the purpose of the quantitative analysis, the sample and its respective tomograms were divided into horizontal layers as depicted in Fig. 5. Layers 1, 3, and 5 were composed of a single

Table 3. Imaging parameters.

Parameter	Drip irrigation experiment	Ponding experiment
Paul Scherrer Institute station†	BOA	NEUTRA
Acquisition time of a radiograph, s	0.25	16
Count of radiograms for one tomogram	461	361
Range of rotation, °	360	180
Acquisition time of a tomogram, min	2	50
Field of view, pixels	512 by 512	1080 by 1280
Pixel size, mm	0.108	0.097

† BOA, Beamline for Neutron Optics and other Approaches; NEUTRA, Neutron Transmission Radiography.

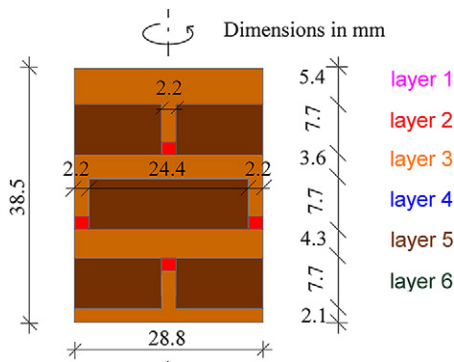


Fig. 5. Schematic of the sample geometry and delimitation of the layers.

material (coarse sand), while Layers 2, 4, and 6 comprised a combination of three materials. The average water content was calculated for each material in all the sample layers with the exception of a layer at the bottom of the sample for which a plastic textile supporting the sample caused a rather heavy artifact due to high attenuation of neutrons.

Replicate Experiments

The experiments were repeated in the laboratory of the Czech Technical University in Prague (CTU) without imaging. The initial and boundary conditions of the experiments were identical to those conducted at the PSI. Two PE and two DE were performed on the same sample. The duration of infiltration to produce outflow in the replicate experiments was longer than in the experiments with concurrent neutron imaging. Two duplicate experiments were performed using “light” water, deionized H₂O kept in an open container before the experiment and thus saturated with air, i.e., aerated. In two additional replicate experiments, degassed water produced by Liqui-Cel Membrane Contactors (3M Company) was used as a liquid medium to enable dissolution of air bubbles in the sample. In case of the DE with the use of degassed water, the sample was first supplied with water at constant flux rate of 1.63 cm h⁻¹ and, after ponding developed, the ponding level was kept at the level of 6 mm above the sample for the rest of the experiment.

Calculation of Hydraulic Conductivity

The hydraulic conductivity (K) of the sample was calculated using Darcy’s law from the measured outflow rate for the duration

of the experiment during which outflow occurred. The flow was not entirely steady for most experiments, but since the boundary conditions were maintained constant and flow rate changes were slow, the observed flow can be regarded as quasi-steady and Darcy’s law considered as applicable. For the purpose of K calculation, the pressure head at the top of the sample was assumed to be equal to the ponding head. The pressure head at the bottom was assumed to be equal to zero, since the bottom of the sample was open to the atmosphere. The hydraulic head gradient was 1.15. Since heavy water and H₂O differ in viscosity and density, the calculated hydraulic conductivity for the experiments done with heavy water was normalized to those values for H₂O. First, the value of the intrinsic permeability k (m²) was calculated using (Constantz, 1982)

$$k = \frac{\mu K}{\rho g} \quad [2]$$

where ρ is the liquid density (kg m⁻³), g is the gravitational acceleration (m s⁻²), μ is the dynamic viscosity of the liquid (N s m⁻²), and K is the saturated hydraulic conductivity (m s⁻¹). The density of D₂O at 25°C is 1104 kg m⁻³, and dynamic viscosity was considered to be 11.0×10^{-4} N s m⁻².

The normalized K for H₂O was then calculated using the same formula (Eq. [2]) considering the density (997 kg m⁻³ at 25°C) and dynamic viscosity (8.9×10^{-4} N s m⁻²) of H₂O. The functions of unsaturated hydraulic conductivity were estimated for all three materials using the van Genuchten–Mualem (VGM) model (van Genuchten, 1980) from measured retention curves and coefficients of saturated hydraulic conductivities.

Results

Two-Dimensional Imaging of Transient Flow

Selected frames of the neutron radiography shown in Fig. 6 illustrate the advancement of the wetting front during the transient flow stage of the DE. Gray shades correspond to the water thickness present in the sample at a given time summed across the sample in the direction of the neutron beam flux, i.e., perpendicular to the image. The outflow did not occur until the end of the experiment (as limited by the beam time available).

It can be clearly seen that the uppermost ceramic disk (Layer 2) became saturated first (see Fig. 6, time 876 s). The overlying coarse

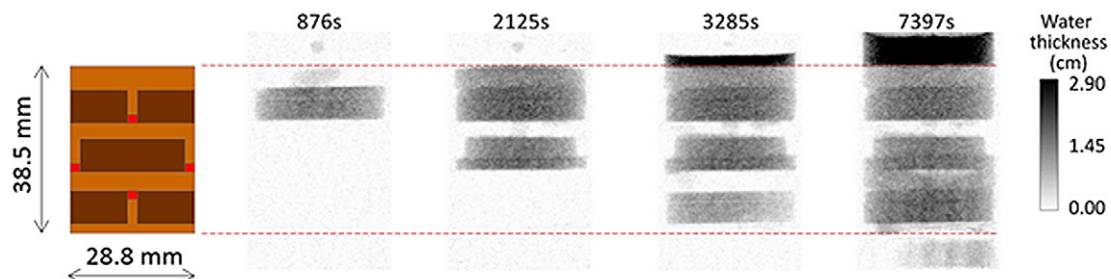


Fig. 6. Radiographs showing the infiltration process in the sample during the drip irrigation infiltration experiment (DE).

sand conducted water quickly to the disk through the narrow path in the center without significantly increasing the water content in Layer 1. Then the middle ceramic disk and the ring of medium sand in Layer 4 absorbed water as the infiltration continued (see Fig. 6, time 2125 s). At this stage, a few connecting flow channels (fingers) developed in the coarse sand of Layer 3 between the uppermost and middle ceramic disks. The same pattern of wetting occurred in the lowest ceramic disk in Layer 6 (see Fig. 6, time 3285 s). As the infiltration continued (see Fig. 6, time 7397 s), the coarse sand in Layer 5 became saturated from the bottom. The air trapped structurally in the coarse sand in Layer 3 prevented any further increase in water content in Layer 3 and blocked the flow to the extent that there was an increase of the ponding depth at the surface after 2700 s of infiltration. The depth of ponding was gradually increasing until the end of the experiment up to a level of 6 mm, the value determined from the raw radiographic projections (not shown in the cropped radiographs in Fig. 6).

In the case of the PE, as can be seen in Fig. 7, the flow patterns were very different from the DE and the water flow was much faster. The coarse sand in Layer 1 and subsequently the ceramic disk in Layer 2 got saturated first. Soon after, due to preferential

flow through the central channel of coarse sand in Layer 2, the ceramic disk in Layer 4 was gradually wetted from the middle while the coarse sand in Layer 3 stayed relatively dry until capillary forces in Layers 3 and 4 restored the equilibrium. When the ceramic disk in Layer 4 became saturated, the medium sand in Layer 4 began to absorb water, thereby trapping air in the coarse sand of Layer 4. Most of the air that was originally present in the coarse sand was being pushed out through the bottom of the sample except for the air located close to the sample walls in Layer 4. The first outflow, detected by a digital scale, occurred 420 s after the start of the infiltration.

Figure 8 shows that image-based water storage in the sample corresponds well to mass-balance-based values. This is also due to the fact that the parameters of Eq. [1] were optimized to achieve the minimum difference between actual and NI-determined water volume.

Three-Dimensional Neutron Tomography

The output of the neutron tomography imaging is a sequence of 25 three-dimensional water content maps for the DE and 15 three-dimensional water content maps for the PE.

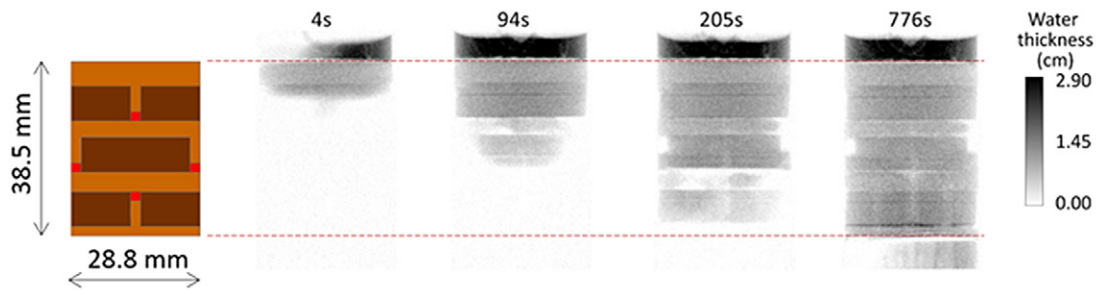


Fig. 7. Radiographs showing the imbibition process in the sample during the ponding infiltration experiment (PE). The area outside of the sample was cropped.

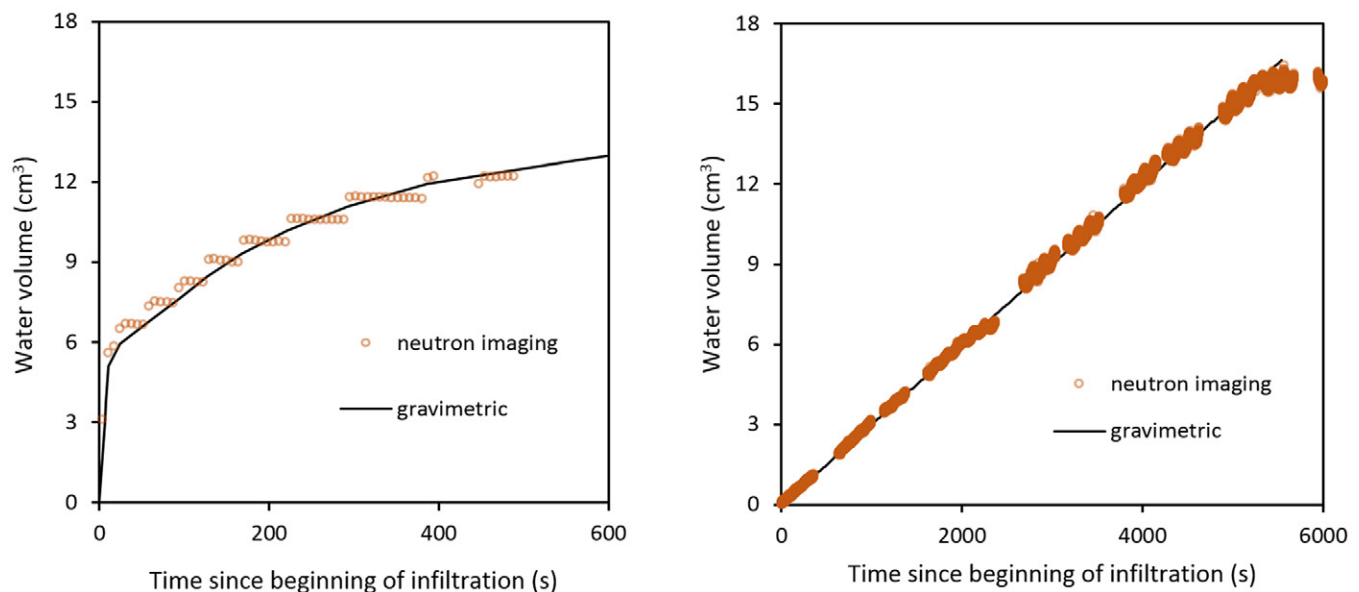


Fig. 8. Comparison of the amount of water cumulatively delivered to the sample determined gravimetrically and by neutron radiography for (a) the ponding infiltration experiment (PE) and (b) the drip irrigation infiltration experiment (DE).

The average water content calculated for each material in the sample layers from three-dimensional water content images are plotted against time in Fig. 9.

Imaging at the BOA allowed faster tomography, and therefore three-dimensional images were taken during the transient flow. In the case of the DE, the three-dimensional imaging confirmed the observations obtained from the two-dimensional radiographs. Generally, the results show that the fine-pore ceramic disks became saturated first. After the partial saturation of the ceramic disks located in Layers 2 and 4, the medium sand in Layer 2 also became wetted. The water flowed through the coarse sand to the lowermost ceramic disk. On the contrary, the coarse sand in Layers 3 and 4 had very low water content during the entire experiment and it is believed that trapped air, especially in Layer 4, was very likely to have restricted the flow of water. A gradual decrease in water content in the coarse sand of Layer 2 was observed after reaching a peak value of 0.5 at 0.3 h after the start of infiltration.

In the case of the PE conducted in the NEUTRA beamline, three-dimensional images were taken only under quasi-steady-state conditions. The PE showed a very rapid increase of water content in all layers as the result of very fast, gravity-driven flow. The coarse sand in Layers 3 and 4 again showed lower water content than the coarse sand in the rest of the sample but still significantly higher than in the DE. In both experiments, a gradual decrease in water content was seen in Layers 3, 4, and 6, and the effect can be explained by a gradual increase of air content in these layers. The water content of the ceramic disks during the PE increased gradually, while in the DE it did not. The dashed lines in Fig. 9 show the saturated water content for each material measured separately on small packed samples. Water content determined by NI was slightly higher than the saturated water content determined separately in some cases (the coarse sand in Layer 1 during the DE and the medium sand in Layer 2 during the PE). It is possible that the packing of these particular layers, mostly close to the top or bottom of the sample, was less dense than in the independent experiment.

Water Fluxes

Water inflow and outflow were continuously monitored during all experiments. In the DE monitored by neutron imaging, outflow did not occur before the end of the assigned beam time. The outflow rate was, however, recorded during the replicated experiments conducted in the CTU laboratory. Figure 10 shows the time development of hydraulic conductivity calculated from the outflow rate for the quasi-steady-state part of the experiments. The first outflow occurred at 3.0 and 3.2 h after the beginning of the experiment. Hydraulic conductivity gradually decreased in all three PEs to the value of nearly one order of magnitude lower than at the beginning of the quasi-steady-state stage of the experiment (Fig. 10). The onset of outflow was earlier than 10 min after the beginning of the infiltration (data were recorded at 10-min intervals in the replicated experiments).

The hydraulic conductivity of the sample was significantly higher in the experiments with degassed water infiltration

in the case of DE (Fig. 11). Probably this was a consequence of better sample saturation due to dissolution of entrapped air. The hydraulic conductivity of the sample during PE with infiltration of degassed water (Fig. 11) exhibits values similar to those detected at the beginning of the replicate experiments, but in the case of degassed water, hydraulic conductivity remained nearly constant.

Discussion

Capillary Barrier Effect

This study is characterized by infiltration of water into an initially dry sample comprising three sample materials of contrasting pore sizes. Under such conditions, the capillary barrier effect can effectively influence the flow (Jansik et al., 2011; Ng et al., 2015; Prédéus et al., 2015). The results of the experiment presented here show that the intensity of capillary barrier formation strongly depends on the inflow rate. These findings are similar to those of the numerical study done by Rudakov (2009), who analyzed the influence of different thicknesses, inclinations, and curvatures of capillary barriers on water transport. He found that lower inflow rates caused less leakage in the parabolic capillary barrier and 0.5-m-thick fine layer. An inflow rate changing from 0.5 mm d^{-1} (0.0021 cm h^{-1}) to 2 mm d^{-1} (0.0083 cm h^{-1}) corresponded to an increase of the leakage from 5 to 9% of the infiltrated amount.

In the experiment presented here, the DE constant inflow flux was 1.63 cm h^{-1} . During the DE, capillarity was the driving force of the water flow at the beginning of the infiltration. Capillary forces acted more strongly on the ceramic disks and medium sand than the coarse sand; therefore in the DE the ceramic disk in Layer 2 became saturated before the other materials. When the ceramic disk became nearly saturated and matric potentials increased, flow continued through the medium sand channel into the coarse sand.

Capillary barrier effects occurred only on the divide between the ceramic disks and the medium and coarse sand. Since there was no inclination in the sample layers, water started to penetrate into the coarse sand in a form of fingers. Figure 12 depicts the formation of fingers in the coarse sand of Layer 3.

During the PE, the capillary barrier effect was minimized by the high inflow rate of approximately 300 cm h^{-1} . The flow was driven mostly by gravity, and all three materials became wet at almost the same time.

Effect of the Wetting Front Inhomogeneity on Air Entrapment

The wetting front observed in the DE was highly uneven due to sequential wetting of the three materials. After some minimal wetting of the coarse sand layer directly below the medium sand, the infiltration was again concentrated into the ceramic disks and then into the medium sand along the perimeter (Fig. 6, time 2 125 s). Air in the coarse sand in Layers 3 and 4 was trapped and was no longer connected to the atmosphere through the top or the bottom of the sample. Such air-entry barriers have often been

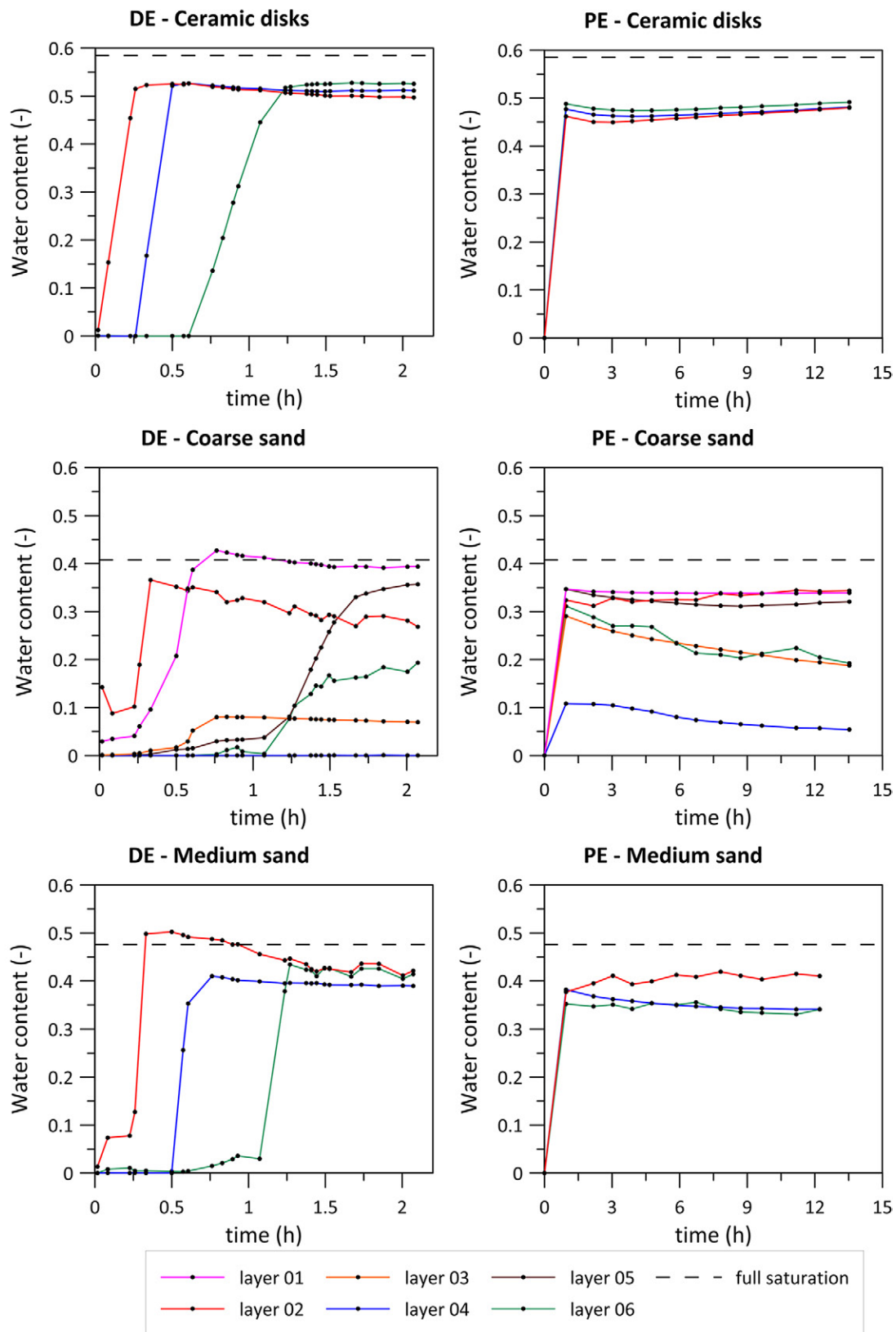


Fig. 9. Neutron tomography derived water content for each layer (colored lines) and each material calculated from tomograms taken during the drip irrigation infiltration experiment (DE) and ponding infiltration experiment (PE). It should be noted that some values of water content, especially in the medium sand material, were determined in very small regions of interest where image noise can play a significant role.

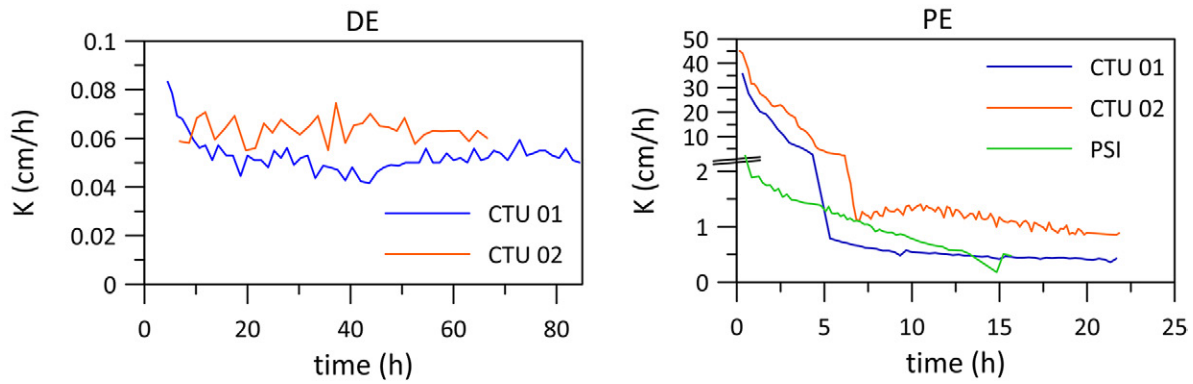


Fig. 10. Time development of hydraulic conductivity of the sample during the drip irrigation infiltration experiment (DE) and the ponding infiltration experiment (PE) during experiments conducted with concurrent neutron imaging (PSI) and during replicate experiments (CTU 01 and CTU 02) conducted with aerated water. Hydraulic conductivity series for the DE with concurrent neutron imaging is omitted because outflow did not occur during the course of the experiment.

observed during drainage processes (Kuang et al., 2011; Silliman et al., 2002), but the current experiment demonstrates that the same effect may occur during downward infiltration. In the DE, the water content of the coarse sand in Layer 3 did not exceed a value of 0.08, which according to the VGM model corresponds to an unsaturated hydraulic conductivity of 0.5 cm h^{-1} (Fig. 9). In Layers 5 and 6, the air entrapment followed a similar pattern but infiltration took place through the medium sand close to walls.

During the PE, the wetting front advanced more evenly, while capillary forces from the ceramic disks still caused their slightly earlier saturation. However, the piston-like flow effectively expelled air from Layers 3 and 4 toward the bottom of the sample. As can be seen in Fig. 7, 97 s after the beginning of infiltration, the water content in Layer 3 reached 0.29 and Layer 4 had a water content of 0.10. It is apparent from the time-lapse tomograms that the ceramic disk absorbed water relatively slowly from its surface inward (not shown here). Consequently, air was probably transferred from the ceramic disk in Layer 4 to the nearby sand for the entire duration of the experiment. This effect seems to be a good example of a local nonequilibrium phenomenon (e.g., Šimůnek et al., 2003; Köhne et al., 2009; Szymkiewicz and Lewandowska, 2006), closely related to preferential flow, because the saturation of the inclusion (ceramic disk) increases with time, while the pressure at the outer surface of the inclusion remains nearly constant.

The water content of the ceramic disk gradually increased, as can be seen in Fig. 9d. Air subsequently accumulated in the coarse sand fraction, especially in Layers 3 and 4, mainly because it could not escape from these layers due to the higher air-entry value of the surrounding materials. Thus, the water content of the coarse sand became less during the course of the continuing infiltration (Fig. 9e), consequently lowering its hydraulic conductivity and the hydraulic conductivity of the whole sample. There is also a possibility of slight mixing of the two sands at the interface. This is mainly true for the coarse and medium sands in Layers 2 and 6. In the case of the sand in Layer 1, the water content derived from the neutron tomograms is higher than its independently measured saturated water content. This is probably due to the neutron scattering effect caused by the large amount of water in the ponding layer immediately above Layer 1. During the experiment with concurrent NI, outflow did not occur before the end of the experiment. The system was, however, very close to saturation at the bottom of the sample.

Effect of Air Entrapment on Hydraulic Conductivity

The relationship between the mean sample water content determined from tomograms and the corresponding hydraulic conductivity determined from fluxes measured during the experiment

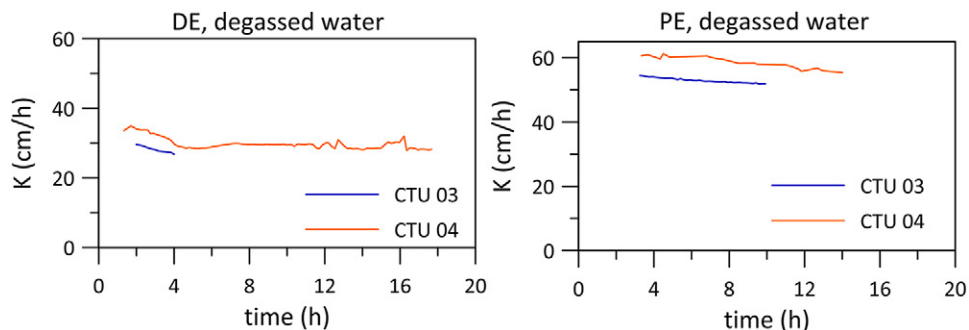


Fig. 11. The time development of hydraulic conductivity (K) after the drip irrigation infiltration experiment (DE) and the ponding infiltration experiment (PE) for infiltration of degassed water.

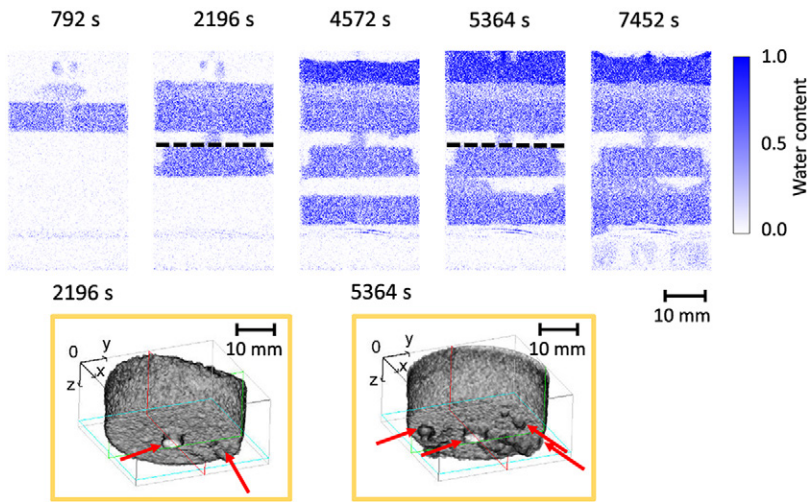


Fig. 12. Vertical slices of the three-dimensional neutron imaging tomograms recorded during the drip irrigation infiltration experiment (DE) (upper), and finger flow recorded during the DE in the sand (Layer 3) below the ceramic disk (Layer 2). Red arrows show the position of the emerging fingers.

is plotted in Fig. 13. The relationship between hydraulic conductivity and water content was determined from tomograms obtained during the steady-state stage of the experiment. The results show that hydraulic conductivity was gradually decreasing, although the mean average water content of the entire sample was almost unchanged. Figure 13 shows that the hydraulic conductivity of the sample determined during the experiments lies between the unsaturated hydraulic conductivity curves of the ceramic and medium sand predicted using the VGM model (van Genuchten, 1980).

Outflow did not occur during the entire 2 h of the DE experiment with concurrent NI, which therefore precluded similar analysis of hydraulic conductivity as was done for the PE. In the case of the DE, the hydraulic conductivity was instead calculated from a replicated experiment with aerated water. The value of the outflow rate detected immediately after achieving steady-state flow was used to calculate the hydraulic conductivity. The corresponding mean water content was derived from the last neutron tomogram of the DE. This approximation is possible because, according to the plots of water content development (Fig. 9a, 9b, and 9c), the water content of all three materials was entirely (medium sand and ceramic) or almost (coarse sand) constant with time; therefore, the capillary forces were already negligible and the only significant driving force was gravity and a positive pressure potential with a total hydraulic head gradient equal to 1.15. The mean water content of the sample determined by this approach is probably slightly underestimated, but it is probably reasonable to assume that the difference is small.

The hydraulic conductivity determined during the steady state of the DE nearly coincides with the predicted unsaturated hydraulic conductivity curve of the ceramic, which corresponds well to the fact that water flowed mainly through the ceramic in this experiment because the coarse sand in the central part of the sample was highly unsaturated due to the presence of entrapped air and therefore was not very conductive. The value of the hydraulic

conductivities measured during the PE lay between the predicted hydraulic conductivity curves of the coarse sand and ceramic disks, close to the hydraulic conductivity curve of the medium sand. This finding corresponds well to the fact that water flowed through all three materials in the PE.

An effective saturated hydraulic conductivity K_{eff} was calculated for times in which the water contents for each layer and material were known. Assuming vertical flow, the hydraulic conductivity of each layer was calculated as the average hydraulic conductivity weighted by the cross-sectional area fraction of each material in the layer. The analogy with Ohm's law (resistors in parallel) used to calculate K_{eff} (Jury et al., 1991) is then

$$K_l = \sum_{i=1}^3 K_i(\theta) f_i \quad [3]$$

$$K_{\text{eff}} = \frac{\sum_{l=1}^n L_l}{\sum_{l=1}^n (L_l / K_l)} \quad [4]$$

where K_l is the effective hydraulic conductivity of l th layer, $K_i(\theta)$ is the hydraulic conductivity predicted from the VGM model (van Genuchten, 1980) for the i th material and its corresponding water content measured by NI in the l th layer, L_l is height of the layer, and f_i is the cross-section fraction of the i th material in the layer.

It is obvious from Fig. 11 that despite the absolute values of the calculated hydraulic conductivity being smaller for the case of the PE than the measured values, the trend was captured reasonably well. The difference in the hydraulic conductivity at the end of the PE and DE was not interpreted well by the calculation.

A ponding layer of water formed atop the sample during the DE because the inflow rate, 1.63 cm h^{-1} , was greater than the hydraulic conductivity of Layer 3, which for a given water content, reached a value of approximately 0.5 cm h^{-1} according to the VGM model. Blockage of the water flow by the highly air saturated Layer 3 is evident in Fig. 9b, where the coarse sand saturates from the bottom up. Layer 2 was apparently saturated earlier than Layer 1.

There was a difference in the absolute values of hydraulic conductivity determined in the two replicated PEs done with aerated water; however, a trend of significant decreases in K with time was apparent in both experiments (Fig. 10). The hydraulic conductivity at the beginning of steady-state flow was significantly higher during the PEs conducted in the CTU laboratory than in the PE with concurrent NI (see Fig. 10, PE). This effect is possibly a result of minute changes to the sample structure during transportation between the Czech Republic and Switzerland, despite the transport having been done carefully.

Summary and Conclusions

A one order of magnitude difference in hydraulic conductivity of the same sample was detected and attributed to different residual gas patterns in infiltration experiments conducted on a

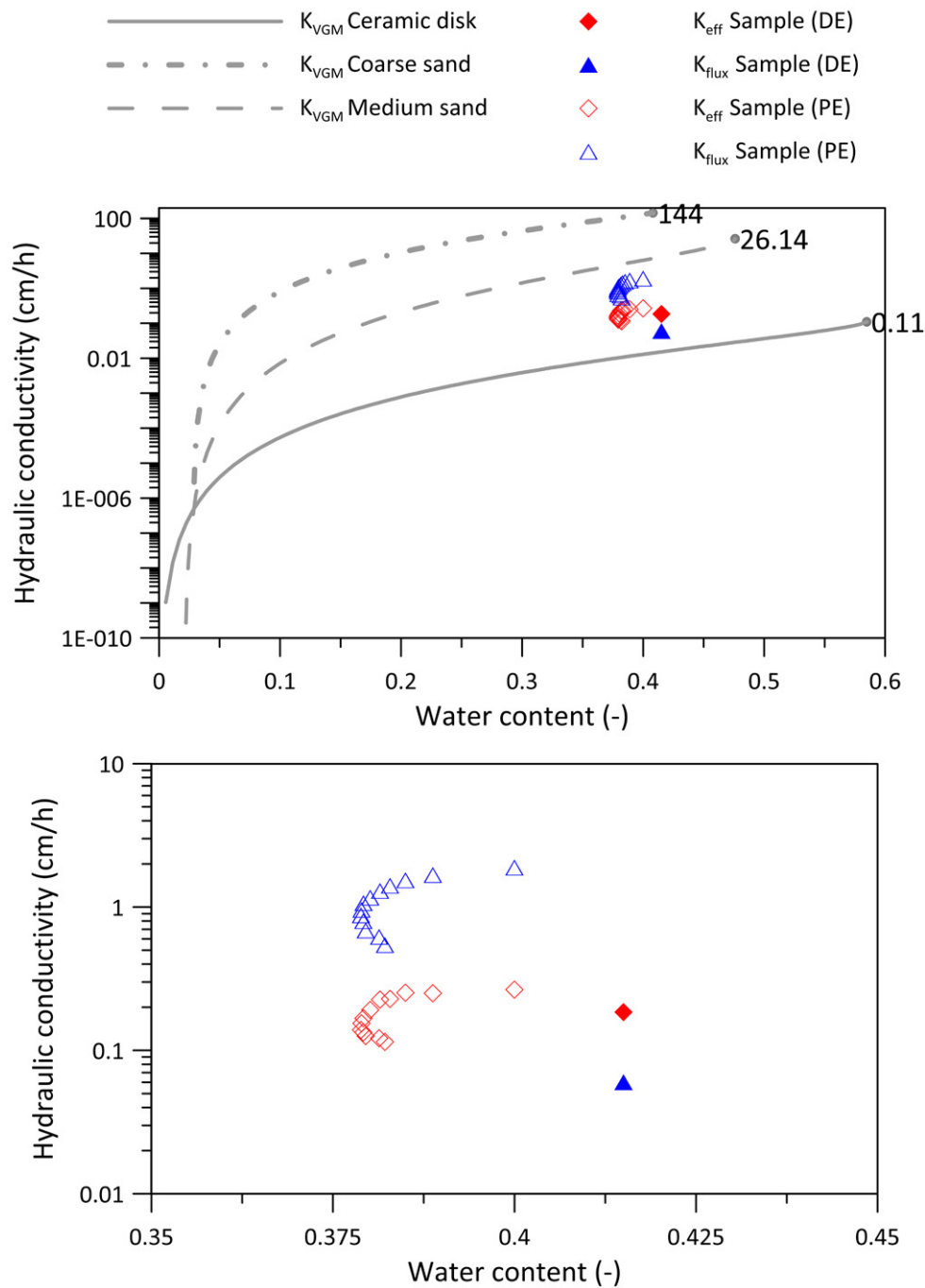


Fig. 13. Hydraulic conductivity curves of the three sample materials predicted using the van Genuchten–Mualem model (K_{VGM}) compared with predicted and measured hydraulic conductivity of the entire sample (symbols). Hydraulic conductivity K_{flux} measured from known fluxes and hydraulic gradients are plotted against water contents derived from neutron tomography imaging (blue triangles); K_{eff} predicted using Eq. [2] and [3] are also plotted against neutron tomography determined water contents (red diamonds). Filled symbols represent the ponding infiltration experiment (PE), empty symbols represent the drip irrigation infiltration experiment (DE). Note that the water content for the DE was estimated from the last acquired tomogram. Overall (upper) and detailed (lower) graphs are shown. Two different hydraulic conductivities for a single water content of the sample are possible due to different water distribution in the sample.

constructed heterogeneous ceramic disk–sand sample. A sequence of neutron tomography imaging of the infiltration process produced quantitatively relevant data on water content in different parts of the sample and indirectly also on air saturation. Slow infiltration dynamics induced by drip irrigation to the top of the sample led to structural trapping of a large amount of air in the

coarse sand regions of the sample. The structural trapping was enhanced by medium sand regions that on wetting disconnected the continuity of the air-filled regions. This led to low hydraulic conductivity of the entire sample and consequently to the development of ponding on the top of the sample. On the contrary, when ponding was deliberately established and maintained at the

beginning of infiltration, a higher water saturation in the coarse sand layers was observed, resulting in a significantly higher hydraulic conductivity estimate for the sample. As a secondary effect, we observed that fast preferential flow through the layers of coarse sand led to higher residual saturation of air in the ceramic disk inclusions. Slow transfer of air from the ceramic disks into the coarse sand due to strong capillary forces attracting water into the ceramic gradually slowed down the flow. A similar effect of reduced infiltration rates has been repeatedly observed in intact soils *in situ* (e.g., Císlerová et al., 1988).

Despite the fact that these effects were demonstrated on a composed sample with a simple material distribution, it is reasonable to assume that the same water flow and air trapping patterns occur in natural heterogeneous soils. The question that should be addressed in follow-up studies is what are the spatial scales at which the phenomenon of flow-dynamics-dependent air trapping is relevant for natural soil systems?

Data Availability

Raw neutron imaging data are available from the Dryad Digital Depository (Sacha et al., 2019).

Acknowledgments

We would like to thank our colleague Dr. Vladka Jelínková for her suggestions on experimental setup design as well for assistance with experiments, and Dr. Lubomir Kopecky for performing the scanning electron microscopy of soil samples. We also would like to thank Prof. Milena Císlerová for invaluable discussions of the experimental results. We would like to thank the two anonymous reviewers for their insightful suggestions and comments that help to significantly improve the manuscript.

Funding for this research was provided by the Czech Science Foundation (Project no. GA17-21011S) and by the Grant Agency of the Czech Technical University in Prague (Grant no. SGS18/122/OHK1/2T/11). This work has been supported by the Ministry of Education, Youth and Sports within National Sustainability Programme I, Project no. LO1605. This work is based on experiments performed at the Swiss Spallation Neutron Source SINQ, Paul Scherrer Institut, Villigen, Switzerland. This research project has been supported by the European Commission under the 7th Framework Programme through the Research Infrastructures action of the Capacities Programme, NMI3-II Grant number 283883, SINQ 20141698.

References

- Badorreck, A., H.H. Gerke, and R.F. Hüttl. 2012. Effects of ground-dwelling beetle burrows on infiltration patterns and pore structure of initial soil surfaces. *Vadose Zone J.* 11(1). doi:10.2136/vzj2011.0109
- Badorreck, A., H.H. Gerke, and R.F. Hüttl. 2013. Morphology of physical soil crusts and infiltration patterns in an artificial catchment. *Soil Tillage Res.* 129:1–8. doi:10.1016/j.still.2013.01.001
- Badorreck, A., H.H. Gerke, and P. Vontobel. 2010. Noninvasive observations of flow patterns in locally heterogeneous mine soils using neutron radiation. *Vadose Zone J.* 9:362–372. doi:10.2136/vzj2009.0100
- Carminati, A., A. Kaestner, R. Hassanein, O. Ippisch, P. Vontobel, and H. Fluhler. 2007. Infiltration through series of soil aggregates: Neutron radiography and modeling. *Adv. Water Resour.* 30:1168–1178. doi:10.1016/j.advwatres.2006.10.006
- Casagrande, A. 1934. *Die Aräometer-Methode zur Bestimmung der Kornverteilung von Böden und anderen Materialien.* Julius Springer, Berlin. doi:10.1007/978-3-642-91247-4
- Cheng, C.L., M. Kang, E. Perfect, S. Voisin, J. Horita, H.Z. Bilheux, et al. 2012. Average soil water retention curves measured by neutron radiography. *Soil Sci. Soc. Am. J.* 76:1184–1191. doi:10.2136/sssaj2011.0313
- Christiansen, J.E. 1944. Effect of entrapped air upon the permeability of soils. *Soil Sci.* 58:355–366. doi:10.1097/00010694-194411000-00002
- Císlerová, M., J. Šimůnek, and T. Vogel. 1988. Changes of steady-state infiltration rates in recurrent ponding infiltration experiments. *J. Hydrol.* 104:1–16. doi:10.1016/0022-1694(88)90154-0
- Constantz, J. 1982. Temperature dependence of unsaturated hydraulic conductivity of two soils. *Soil Sci. Soc. Am. J.* 46:466–470. doi:10.2136/sssaj1982.03615995004600030005x
- Debacker, L.W. 1967. Measurement of entrapped gas in study of unsaturated flow phenomena. *Water Resour. Res.* 3:245–249. doi:10.1029/WR003i001p00245
- de Beer, F.C., and M.F. Middleton. 2006. Neutron radiography imaging, porosity and permeability in porous rocks. *S. Afr. J. Geol.* 109:541–550. doi:10.2113/gssajg.109.4.541
- Dekker, L.W., C.J. Ritsema, K. Oostindie, and O.H. Boersma. 1998. Effect of drying temperature on the severity of soil water repellency. *Soil Sci.* 163:780–796. doi:10.1097/00010694-199810000-00002
- Dohnal, M.V., M. Jelínková, J. Snehota, J. Dušek, and J. Březina. 2013. Tree-dimensional numerical analysis of water flow affected by entrapped air: Application of noninvasive imaging techniques. *Vadose Zone J.* 12(1). doi:10.2136/vzj2012.0078
- Dunn, A.M., and S.E. Silliman. 2003. Air and water entrapment in the vicinity of the water table. *Groundwater* 41:729–734. doi:10.1111/j.1745-6584.2003.tb02414.x
- Faybishenko, B.A. 1995. Hydraulic behavior of quasi-saturated soils in the presence of entrapped air: Laboratory experiments. *Water Resour. Res.* 31:2421–2435. doi:10.1029/95WR01654
- Fischer, W.E. 1996. SINQ: The spallation neutron source, a new research facility at PSI. *AIP Conf. Proc.* 392:1119–1122. doi:10.1063/1.52691
- Geistlinger, H., A.D. Iman, M. Sadjad, and H.J. Vogel. 2015. The impact of pore structure and surface roughness on capillary trapping for 2-D and 3-D porous media: Comparison with percolation theory. *Water Resour. Res.* 51:9094–9111. doi:10.1002/2015WR017852
- Hassanein, R., F. de Beer, N. Kardjilov, and E. Lehmann. 2006a. Scattering correction algorithm for neutron radiography and tomography tested at facilities with different beam characteristics. *Physica B* 385–386:1194–1196. doi:10.1016/j.physb.2006.05.406
- Hassanein, R., H.O. Meyer, A. Carminati, M. Estermann, E. Lehmann, and P. Vontobel. 2006b. Investigation of water imbibition in porous stone by thermal neutron radiography. *J. Phys. D: Appl. Phys.* 39:4284. doi:10.1088/0022-3727/39/19/023
- Jansik, D.P., D. Wildenschild, and N.D. Rosenberg. 2011. Flow processes in the dry regime: The effect on capillary barrier performance. *Vadose Zone J.* 10:1173–1184. doi:10.2136/vzj2010.0128
- Jury, W.A., W.R. Gardner, and W.H. Gardner. 1991. *Soil physics.* 5th ed. John Wiley & Sons, New York.
- Kaestner, A.P. 2011. Muhrec: A new tomography reconstructor. *Nucl. Instrum. Methods Phys. Res., Sect. A* 651:156–160. doi:10.1016/j.nima.2011.01.129
- Kaestner, A.P., P. Trtik, M. Zarebanadkouki, D. Kazantsev, M. Snehota, K.J. Dobson, and E.H. Lehmann. 2016. Recent developments in neutron imaging with applications for porous media research. *Solid Earth* 7:1281–1292. doi:10.5194/se-7-1281-2016
- Kang, M., H.Z. Bilheux, S. Voisin, C.L. Cheng, E. Perfect, J. Horita, and J.M. Warren. 2013. Water calibration measurements for neutron radiography: Application to water content quantification in porous media. *Nucl. Instrum. Methods Phys. Res., Sect. A* 708:24–31. doi:10.1016/j.nima.2012.12.112
- Klute, A. 1986. Water retention: Laboratory methods. In: A. Klute, editor, *Methods of soil analysis. Part 1. Physical and mineralogical methods.* 2nd ed. SSSA and ASA, Madison, WI. p. 635–662. doi:10.2136/sssabookser5.1.2ed.c26
- Köhne, J.M., S. Köhne, and J. Šimůnek. 2009. A review of model applications for structured soils: A. Water flow and tracer transport. *J. Contam. Hydrol.* 104:4–35. doi:10.1016/j.jconhyd.2008.10.002
- Kuang, X.X., J.J. Jiao, L. Wan, X.S. Wang, and D.Q. Mao. 2011. Air and water flows in a vertical sand column. *Water Resour. Res.* 47:W04506. doi:10.1029/2009WR009030
- Lehmann, E., P. Vontobel, and L. Wiezel. 2001. Properties of the radiography facility NEUTRA at SINQ and its potential for use as

- European reference facility. *Nondestruct. Test. Eval.* 16:191–202. doi:10.1080/10589750108953075
- Lehmann, P., P. Wyss, A. Flisch, E. Lehmann, P. Vontobel, M. Krafczyk, et al. 2006. Tomographical imaging and mathematical description of porous media used for the prediction of fluid distribution. *Vadose Zone J.* 5:80–97. doi:10.2136/vzj2004.0177
- Loizeau, S., Y. Rossier, J.P. Gaudet, A. Refloch, K. Besnard, R. Angulo-Jaramillo, and L. Lassabatere. 2017. Water infiltration in an aquifer recharge basin affected by temperature and air entrapment. *J. Hydrol. Hydromech.* 65:222–233. doi:10.1515/johh-2017-0010
- Menon, M., B. Robinson, S.E. Oswald, A. Kaestner, K.C. Abbaspour, E. Lehmann, and R. Schulin. 2007. Visualization of root growth in heterogeneously contaminated soil using neutron radiography. *J. Soil Sci.* 58:802–810. doi:10.1111/j.1365-2389.2006.00870.x
- Moradi, A.B., H.M. Conesa, B. Robinson, E. Lehmann, G. Kuehne, A. Kaestner, et al. 2009. Neutron radiography as a tool for revealing root development in soil: Capabilities and limitations. *Plant Soil* 318:243–255. doi:10.1007/s11104-008-9834-7
- Morgano, M., S. Peetermans, E. H. Lehmann, T. Panzner, and U. Filges. 2014. Neutron imaging options at the BOA beamline at Paul Scherrer Institut. *Nucl. Instrum. Methods Phys. Res., Sect. A* 754:46–56. doi:10.1016/j.nima.2014.03.055.
- Ng, C.W.W., J. Liu, R. Chen, and J. Xu. 2015. Physical and numerical modeling of an inclined three-layer (silt/gravelly sand/clay) capillary barrier cover system under extreme rainfall. *Waste Manage.* 38:210–221. doi:10.1016/j.wasman.2014.12.013
- Oldenburg, C.M., and K. Pruess. 1993. On numerical modeling of capillary barriers. *Water Resour. Res.* 29:1045–1056. doi:10.1029/92WR02875
- Oswald, S.E., M. Menon, A. Carminati, P. Vontobel, E. Lehmann, and R. Schulin. 2008. Quantitative imaging of infiltration, root growth, and root water uptake via neutron radiography. *Vadose Zone J.* 7:1035–1047. doi:10.2136/vzj2007.0156
- Perfect, E., C.L. Cheng, M. Kang, H.Z. Bilheux, J.M. Lamanna, M.J. Gragg, and D.M. Wright. 2014. Neutron imaging of hydrogen-rich fluids in geomaterials and engineered porous media: A review. *Earth Sci. Rev.* 129:120–135. doi:10.1016/j.earscirev.2013.11.012
- Prédélus, D., A.P. Coutinho, L. Lassabatere, L.B. Bien, T. Winiarski, and R. Angulo-Jaramillo. 2015. Combined effect of capillary barrier and layered slope on water, solute and nanoparticle transfer in an unsaturated soil at lysimeter scale. *J. Contam. Hydrol.* 181:69–81. doi:10.1016/j.jconhyd.2015.06.008
- Ray, C., C. Miyasaki, M. Snehota, L. Sharma, and M. Sanda. 2010. Alternative methods to control water infiltration for landfills: A case study in the tropics. *Int. J. Environ. Technol. Manage.* 13:37–50. doi:10.1504/IJETM.2010.038016
- Reynolds, W.D., and D.E. Elrick. 1986. A method for simultaneous in situ measurement in the vadose zone of field-saturated hydraulic conductivity, sorptivity and the conductivity–pressure head relationship. *Groundwater Monit. Rem.* 6:84–95. doi:10.1111/j.1745-6592.1986.tb01229.x
- Richards, L.A. 1931. Capillary conduction of liquids through porous mediums. *Physics* 1:318–333. doi:10.1063/1.1745010
- Roosevelt, S.E., and M.Y. Corapcioglu. 1998. Air bubble migration in a granular porous medium: Experimental studies. *Water Resour. Res.* 34:1131–1142. doi:10.1029/98WR00371
- Rudakov, D. 2009. Numerical modelling of water transport in capillary barriers of different form. *Arch. Min. Sci.* 54:381–391.
- Šácha, J., and M. Sněhota. 2016. Quantitative evaluation of water distribution in the soil sample using neutron imaging. *Acta Polytech.* 56:388–394. doi:10.14311/AP.2016.56.0388
- Sacha, J., M. Snehota, P. Trtik, and J. Hovind. 2019. Data from: Impact of infiltration rate on residual air distribution and hydraulic conductivity. Dryad Digital Repository. doi:10.5061/dryad.g8q382h
- Schaap, J.D., P. Lehmann, A. Kaestner, P. Vontobel, R. Hassanein, G. Frei, et al. 2008. Measuring the effect of structural connectivity on the water dynamics in heterogeneous porous media using speedy neutron tomography. *Adv. Water Resour.* 31:1233–1241. doi:10.1016/j.advwatres.2008.04.014
- Shokri, N., P. Lehmann, and D. Or. 2010. Evaporation from layered porous media. *J. Geophys. Res.* 115:B06204. doi:10.1029/2009JB006743
- Silliman, S.E., B. Berkowitz, J. Šimůnek, and M.Th. van Genuchten. 2002. Fluid flow and solute migration within the capillary fringe. *Groundwater* 40:76–84. doi:10.1111/j.1745-6584.2002.tb02493.x
- Šimůnek, J., N.J. Jarvis, M.Th. van Genuchten, and A. Gärdenäs. 2003. Review and comparison of models for describing non-equilibrium and preferential flow and transport in the vadose zone. *J. Hydrol.* 272:14–35. doi:10.1016/S0022-1694(02)00252-4
- Sněhota, M., M. Císlarová, M.H.G. Amin, and L.D. Hall. 2010. Tracing the entrapped air in heterogeneous soil by means of magnetic resonance imaging. *Vadose Zone J.* 9:373–384. doi:10.2136/vzj2009.0103
- Snehota, M., V. Jelinkova, M. Sobotkova, J. Sacha, P. Vontobel, and J. Hovind. 2015. Water and entrapped air redistribution in heterogeneous sand sample: Quantitative neutron imaging of the process. *Water Resour. Res.* 51:1359–1371. doi:10.1002/2014WR015432
- Soares, M.I.M., S. Belkin, and A. Abeliovich. 1988. Biological groundwater denitrification: Laboratory studies. *Water Sci. Technol.* 20:189–195. doi:10.2166/wst.1988.0098
- Szymańska, P., W. Tisler, C. Schütz, A. Szymkiewicz, I. Neuweiler, and R. Helmig. 2016. Experimental and numerical analysis of air trapping in a porous medium with coarse textured inclusions. *Acta Geophys.* 64:2487–2509. doi:10.1515/acgeo-2016-0095
- Szymkiewicz, A., R. Helmig, and I. Neuweiler. 2012. Upscaling unsaturated flow in binary porous media with air entry pressure effects. *Water Resour. Res.* 48:W04522. doi:10.1029/2011WR010893
- Szymkiewicz, A., and J. Lewandowska. 2006. Unified macroscopic model for unsaturated water flow in soils of bimodal porosity. *Hydrol. Sci. J.* 51:1106–1124. doi:10.1623/hysj.51.6.1106
- Tötze, C., N. Kardjilov, I. Manke, and S.E. Oswald. 2017. Capturing 3D water flow in rooted soil by ultra-fast neutron tomography. *Sci. Rep.* 7:6192. doi:10.1038/s41598-017-06046-w
- Tsimpanogiannis, I.N., and Y.C. Yortsos. 2002. Model for the gas evolution in a porous medium driven by solute diffusion. *AIChE J.* 48:2690–2710. doi:10.1002/aic.690481126
- van Genuchten, M.Th. 1980. A closed-form equation for predicting the hydraulic conductivity of unsaturated soil. *Soil Sci. Soc. Am. J.* 44:892–898. doi:10.2136/sssaj1980.03615995004400050002x
- van Genuchten, M.Th., F.J. Leij, and S.R. Yates. 1991. The RETC code for quantifying the hydraulic functions of unsaturated soils, Version 1.0. EPA Rep. 600/2-91/065. US Salinity Lab., Riverside, CA.
- Vasin, M., P. Lehmann, A. Kaestner, R. Hassanein, W. Nowak, R. Helmig, and I. Neuweiler. 2008. Drainage in heterogeneous sand columns with different geometric structures. *Adv. Water Resour.* 31:1205–1220. doi:10.1016/j.advwatres.2008.01.004
- Yakirevich, A., T.J. Gish, J. Šimůnek, M.Th. van Genuchten, Y.A. Pachepsky, T.J. Nicholson, and R.E. Cady. 2010. Potential impact of a seepage face on solute transport to a pumping well. *Vadose Zone J.* 9:686–696. doi:10.2136/vzj2009.0054
- Zarebanadkouki, M., A. Carminati, A. Kaestner, D. Mannes, M. Morgano, S. Peetermans, et al. 2015. On-the-fly neutron tomography of water transport into lupine roots. *Phys. Procedia* 69:292–298. doi:10.1016/j.phpro.2015.07.041
- Zarebanadkouki, M., E. Kroener, A. Kaestner, and A. Carminati. 2014. Visualization of root water uptake: Quantification of deuterated water transport in roots using neutron radiography and numerical modeling. *Plant Physiol.* 166:487–499. doi:10.1104/pp.114.243212
- Zboray, R., and P. Trtik. 2018. 800 fps neutron radiography of air–water two-phase. *MethodsX* 5:96–102. doi:10.1016/j.mex.2018.01.008
- Zhang, Y.S., and R.K. Gillham. 2005. Effects of gas generation and precipitates on performance of Fe⁰ PRBs. *Groundwater* 43:113–121. doi:10.1111/j.1745-6584.2005.tb02290.x
- Zlotnik, V.A., D.E. Eisenhauer, D.J. Schlautman, B.R. Zurbuchen, and D. Van Peurse. 2007. Entrapped air effects on dipole flow test in sand tank experiments: Hydraulic conductivity and head distribution. *J. Hydrol.* 339:193–205. doi:10.1016/j.jhydrol.2007.03.013